Radiation-induced Attenuation in Standard Optical Fibers at Cryogenic Temperatures: Effect of Photobleaching Wavelength/Energy

Joseph J. Schuyt, Fernando Solis Fernandez, Shahna M. Haneef, Dominic A. Moseley, *Member*, *IEEE*, Bartholomew M. Ludbrook, *Member*, *IEEE*, Rodney A. Badcock, *Fellow*, *IEEE*

***Abstract*—The low temperature (cryogenic) irradiation of optical fibers produces severe radiation-induced attenuations (RIA) that limit the functionalities and lifetimes of fiber-based sensors. The RIA at some primary probe wavelength (e.g., 1550 nm) can be mitigated via photobleaching with light of some secondary wavelength (e.g., 1050 nm), increasing the lifetimes of such sensing systems. Herein, we investigated the effects of four different photobleaching wavelengths (1050 nm, 880 nm, 770 nm, and 450 nm) on the RIA growth kinetics and the saturation RIA in standard optical fibers (SMF28e+) irradiated at 15 K. The photobleaching was most effective for 770 nm light and least effective for 450 nm light. The latter was negatively impacted by significant attenuation of the photobleaching light itself. The data were analyzed using a kinetic model, through which the photobleaching rates per input power, as a function of photon energy, were calculated.**

***Index Terms*—Cryogenic, irradiation, optical fiber, photobleaching, radiation-induced attenuation.**

I. INTRODUCTION

THE implementation of fiber optic systems, including transmission lines and sensors, in ionizing radiation environments is difficult due to radiation-induced attenuation (RIA) phenomena. When optical fibers are exposed to ionizing radiations (e.g., high energy neutrons, gamma rays, X-rays), numerous absorptive defects are produced that span a very wide spectral range [1]. As these defects absorb light along the fiber core, the signals-of-interest may be attenuated, preventing accurate measurements and/or data transmission. Thus, the severity of the RIA in particular fibers under particular conditions limits the useful lifetime, and overall viability, of fiber-based systems. In most types of optical fiber, the RIA at low temperatures is much greater than that at room temperature [2–8]. Consequently, the development of fiber systems viable for use in cryogenic, radiation-rich environments, such as HTS magnets in fusion reactors [9,10] and spacecraft [11], is a significant challenge.

There are three major mechanisms through which RIA can be reduced: thermal annealing, chemical hardening, and photobleaching. Radiation-induced defects can be thermally annealed [12,13], which requires that the fibers are either irradiated at high temperatures or that the fibers are thermally cycled to high temperatures between irradiation periods. Generally, this technique is not practical in a cryogenic context. Radiation-hard fibers can be manufactured via control of the chemical composition of the fibers [14]. For example, at room temperature, F-doped fibers exhibit RIA two orders of magnitude lower than that of Ge-doped fibers when irradiated with high doses [7,8]. However, even radiation-hard fibers exhibit significant RIA when irradiated at cryogenic temperatures [7].

The most promising technique for low temperature RIA mitigation is photobleaching, whereby light transmitted through the fiber core is itself used to inhibit the stable formation of radiation-induced defects [15–21]. This is usually achieved by increasing the intensity of the primary probe light and/or injecting additional light at some secondary wavelength distinct to the probe wavelength. The overall effectiveness of photobleaching depends on the monitored wavelength, the irradiation temperature, the fiber composition, the wavelength and power of the photobleaching light, and the length of the irradiated fiber [15–21]. As conventional silica fibers are designed to operate in the C-band (1530 nm – 1565 nm), the RIA near 1550 nm is of the greatest practical importance. Recent works have demonstrated that photobleaching with shorter wavelength light effectively reduces the RIA at 1550 nm at low temperatures [15,18,20], where shorter wavelengths are generally more effective. It is therefore of interest to investigate the effects of different wavelengths of photobleaching light on the 1550 nm RIA at cryogenic temperatures, toward the optimization of future photobleaching-based fiber optic systems.

In recent related works [22,23] we developed and validated a model through which high dose RIA values can be predicted as a function of irradiation dose rate, temperature, and photobleaching power. In doing so, we devised a method through which the photobleaching rates, as a function of input power, can be calculated from experimental data. Herein, we characterized the RIA at 1550 nm of standard optical fibers (Corning SMF28e+) at 15 K up to doses of approximately 400

This work was supported by the New Zealand Ministry of Business, Innovation, and Employment (MBIE) Catalyst Fund under RTVU1916. FSF acknowledges support from the Dodd-Walls Center Output Award. We thank Bill Trompetter (GNS) for assistance with radiation safety and operation.

J.J.S. and F.F.S. contributed equally to this work. *Corresponding author: Joseph J. Schuyt. Email: joe.schuyt@vuw.ac.nz*.

The authors are with the Paihau–Robinson Research Institute, Victoria University of Wellington, Lower Hutt 5046, New Zealand. J.J.S., F.S.F., S.M.H., B.M.L., and R.A.B., are also with Te Whai Ao – Dodd-Walls Center for Photonic and Quantum Technologies, Lower Hutt 5046, New Zealand. R.A.B., is also with OpenStar Technologies, Wellington 6035, New Zealand.

Color versions of one or more of the figures in this article are available online at http://ieeexplore.ieee.org

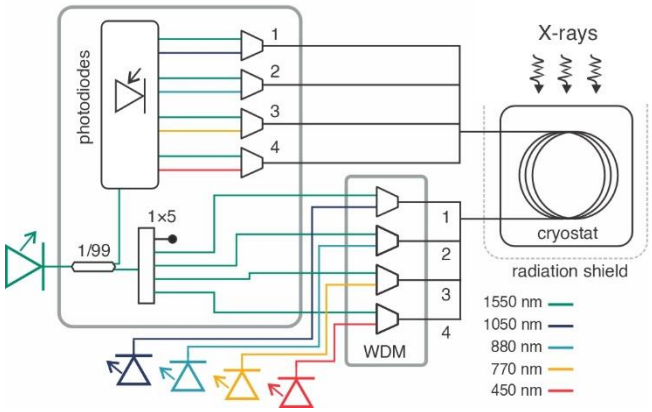

Fig. 1. Schematic of the experimental setup. X/Y and X×Y = fiber splitters, WDM = wavelength division multiplexer.

kGy in fibers with different photobleaching wavelengths (1050 nm, 880 nm, 770 nm, and 450 nm). We demonstrate that photobleaching efficacy strongly depends on the wavelength of the photobleaching light. However, attenuation of the photobleaching light itself can significantly reduce the photobleaching efficacy.

II. Experimental

Multiple optical fibers were concurrently irradiated with steady-state X-rays in the Cryogenic Irradiation of Superconductors and Optical Fibres Laboratory (CRISOL) facility at Paihau-Robinson Research Institute, NZ. Fibers were wound about a copper bobbin mounted on the coldhead of a custom-built cryostat, with a small amount of Apiezon N vacuum grease between each layer to ensure good thermal contact and to minimize strain effects. The radiation-facing side of the cryostat was constructed of 0.5 mm thick aluminum. The fiber temperature was monitored via a Cernox thermometer attached to the copper mount. The X-ray source was a Comet MXR 321 with a tungsten target that was operated at 320 kV. When operated at the maximum current, the dose rate to Ge-doped fibers is 8.7 Gy s^{-1} [16].

The experiment used the optical configuration shown in Fig. 1. The fiber temperature was maintained at 15 K throughout. The target dose rate was Φ = 8.7 Gy s^{-1} for the entire experiment. However, the source required a seasoning procedure, where the voltage and current were slowly ramped to their maximum values. Thus, the dose rate was steadily increased over the first ~1 hour of irradiation before reaching the maximum. Four distinct samples cut to lengths of approximately 2 m, from a single batch of Corning SMF28e+ standard fiber, were irradiated. The 1550 nm probe light source was a Thorlabs S5FC1005S superluminescent diode (SLD), the output of which was first split by a 1/99 coupler. The 1% reference signal was directed to a photodiode. The remaining signal was split and coupled into the sample fibers via 980 nm/1550 nm wavelength division multiplexers (WDMs) (Thorlabs WD9850AB). Photobleaching lights with nominal peaks at 1050 nm, 880 nm, and 770 nm were supplied by additional SLDs (Thorlabs SLD1050S, Thorlabs SLD880S-A7, and Thorlabs SLD770S, respectively). Photobleaching light at 450 nm was supplied by a fiber-coupled laser

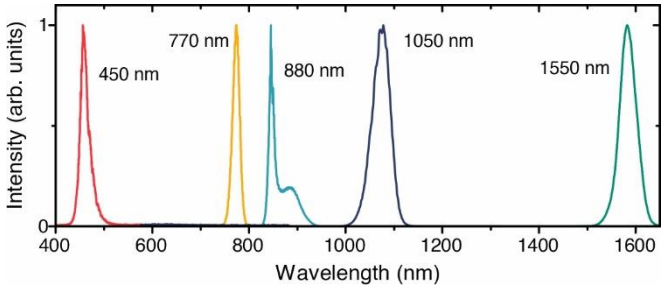

Fig. 2. Emission spectra of the various SLDs used in this work, labeled per their nominal peak wavelengths.

(Tonifishi FJ450A13: core diameter 105 μm, NA 0.22, maximum power 3 W).

The measured emission spectra of the various sources are shown in Fig. 2. The nominal and measured peak wavelengths differed for all sources. Regardless, we refer to each source by its nominal peak throughout this article. The photobleaching light was coupled into the sample fibers via the same WDMs. After transmission through the fiber samples, the coupled light was decoupled using similar WDMs and subsequently routed to photodiodes. All photodiodes (Thorlabs FGA01FC) were connected to transimpedance amplifiers, and the outputs were read and digitized via NI-9205 card.

As the WDMs were not designed for the wavelengths used in the experiment, we characterized the losses and crosstalk at each wavelength. At 1050 nm, 880 nm, and 770 nm, the WDMs functioned well, where generally ≲1% of the photobleaching input co-propagated with the 1550 nm probe light, and vice versa. As WDMs were employed both before and after the fiber samples, the cumulative crosstalk was negligible. The InGaAs photodiodes employed were entirely insensitive to the 450 nm light, meaning all detected light corresponded to the 1550 nm signal. Prior to irradiation, the optical powers at 1550 nm (P_{1550}) and at various photobleaching wavelengths (P_λ, λ_{PB} = 1050 nm, 880 nm, 770 nm) at the cryostat connectors were measured via power meter (Thorlabs S155C). These powers are given in Table I. The 450 nm and 770 nm outputs were also measured via CCD spectrometer, and the 450 nm output was controlled such that the peak intensities of the two outputs were approximately equivalent. Then, the 450 nm input power was approximately equivalent to that at 770 nm, on the order of several mW.

TABLE I
PROBE AND PHOTOBLEACHING OPTICAL POWERS AND NOMINAL (MEASURED) PEAK WAVELENGTHS

Fiber	1	2	3	4
P_{1550} (mW)	0.81	0.45	2.15	2.24
λ_{PB} (nm)	1050 (1072)	880 (865)	770 (773)	450 (463)
P_λ (mW)	4.15	1.12	3.41	~3

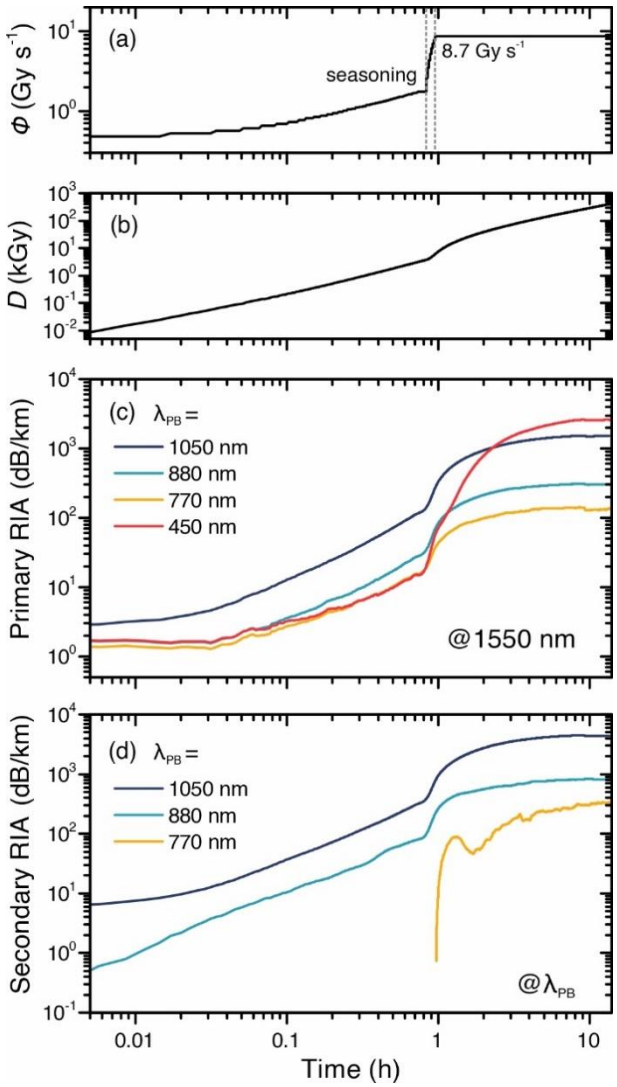

Fig. 3. Experimental results: (a) dose rate as a function of time; (b) cumulative dose as a function of time; (c) Primary RIA at 1550 nm for different photobleaching wavelengths λ_{PB} as a function of time; (d) Secondary RIA at each photobleaching wavelength as a function of time.

III. Results

The experimental results are shown in Fig. 3. The dose rate changed significantly in the early stages of the experiment, during the seasoning procedure (Fig. 3a). We therefore separate the results into three distinct periods of irradiation: early-stage seasoning ($t \lesssim 0.73$ h), late-stage seasoning (0.73 h $\lesssim t \lesssim$ 0.95 h), and high-dose irradiation ($t >$ 0.95 h). The cumulative dose received by each fiber over the course of the experiment is shown in Fig. 3b. The RIA was measured at 1550 nm in all fibers, which is henceforth referred to as the *primary* RIA (Fig. 3c). The RIA was also measured at each secondary photobleaching wavelength, except for λ_{PB} = 450 nm (Fig. 3d). We henceforth refer to the RIA at each photobleaching wavelength as the *secondary* RIA.

Early-stage seasoning: During this period, the voltage of the X-ray source was steadily increased to its maximum. The dose rates and cumulative doses were small, relative to the later stages. The primary RIA values were on the order of several dB/km for all fibers and increased as the cumulative dose increased. Notably, the primary RIA where λ_{PB} = 1050 nm was several times larger than all other primary RIA values. The secondary RIA values for λ_{PB} = 1050 nm and 880 nm were qualitatively similar, though the former were approximately 3× larger for most of the period. Also, the secondary RIA values were larger than the primary RIA values for most of the period. Secondary RIA values could not be accurately calculated for λ_{PB} = 770 nm as the variations in the transmitted power were within the system noise.

The primary and secondary RIA values obtained for each fiber at the end of the early-stage seasoning period, corresponding to a cumulative dose of 3.1 kGy, are given in Table II.

Late-stage seasoning: During this period, the current of the X-ray source was steadily increased to its maximum. The dose rate increased from 1.7 Gy s^{-1} to 8.7 Gy s^{-1}. Both the primary and secondary RIAs increased rapidly. The relative increase was largest for the primary RIA when λ_{PB} = 450 nm. The relative magnitudes of the primary and secondary RIAs for all other λ_{PB} were similar to those observed during early-stage seasoning.

The primary and secondary RIA values obtained for each fiber at the end of the late-stage seasoning period, corresponding to a cumulative dose of 6 kGy, are given in Table II.

High-dose irradiation: During this period, the dose rate was constant (8.7 Gy s^{-1}), and the fibers were continuously irradiated for approximately 12 hours. The primary RIA in all fibers increased monotonically with cumulative dose and trended toward constant (*saturation*) values. The primary RIA growth rates for λ_{PB} = 1050 nm, 880 nm, and 770 nm were qualitatively similar, though the magnitude of the RIA was smaller for shorter secondary wavelengths. The primary RIA growth curve for λ_{PB} = 450 nm was unique, exhibiting several points of inflection over the first few hours. Further, the RIA at the start of the period was similar to that of λ_{PB} = 880 nm, and the RIA at the end of the period was almost twice that of λ_{PB} = 1050 nm. Thus, the relative primary RIA increase for λ_{PB} = 450 nm was much larger than for all other λ_{PB}. The secondary RIA in all fibers also increased monotonically with cumulative dose and trended toward saturation values. However, the growth rates were qualitatively dissimilar for different λ_{PB}. The secondary RIA at 770 nm was noisy due to the weak absorption at low cumulative doses. We note the discontinuity observed in all primary and secondary RIA data at $t \approx$ 9.2 h, which we attribute to an experimental artifact likely induced by a fluctuation in the X-ray source current (i.e., the dose rate). This feature does not significantly influence the results and is ignored in all subsequent analyses.

The primary and secondary RIA values obtained for each fiber at the end of the high-dose irradiation period, corresponding to a cumulative dose of ~400 kGy, are given in Table II.

TABLE II
PRIMARY (1550 NM) RIA AND SECONDARY (λ_{PB}) RIA MEASURED AT THE END OF EACH IRRADIATION PERIOD

Fiber (λ_{PB})	1 (1050 nm)	2 (880 nm)	3 (770 nm)	4 (450 nm)
Primary (1550 nm) RIA (dB/km):				
Early-stage seasoning (3 kGy)	116	28	16	15
Late-stage seasoning (6 kGy)	270	69	37	57
High-dose irradiation (400 kGy)	1505	302	134	2590
Secondary (λ_{PB}) RIA (dB/km):				
Early-stage seasoning (3 kGy)	318	81	-	-
Late-stage seasoning (6 kGy)	768	216	-	-
High-dose irradiation (400 kGy)	4326	795	326	-

IV. DISCUSSION

The primary purpose of this work was to investigate the effects of different secondary wavelengths on the primary RIA during heavy irradiation. Consequently, all subsequent analyses and discussions focus on the data obtained during the high-dose irradiation period. The primary RIA measured in each fiber over this period is shown in Fig. 4a and the secondary RIA is shown in Fig. 4b.

First, we evaluated the relative photobleaching efficacy of each secondary wavelength in terms of the high-dose, nearly saturated RIA at 1550 nm, as measured at the end of the high-dose irradiation period (Table II). These RIA values are representative of equilibrated fiber systems in which the defect generation and bleaching rates are balanced [22] and are therefore representative of the upper limit RIA values under the specific experimental conditions. The final RIA was smallest for λ_{PB} = 770 nm, which was 2× smaller than that obtained for λ_{PB} = 880 nm, 10× smaller than that obtained for λ_{PB} = 1050 nm, and 20× smaller than that obtained for λ_{PB} = 450 nm. As the photobleaching powers were similar for all λ_{PB} (several mW), these results demonstrate that the specific wavelength of the photobleaching light has a pronounced effect on the equilibrated RIA.

The efficacy of the 770 nm photobleaching light can be benchmarked by comparison to the case of zero photobleaching (i.e., several mW of 1550 nm light, no secondary light) [23]. Under these conditions, and in the same fibers at 15 K, the saturation RIA at 1550 nm is approximately 6000 dB/km. Here, the saturation RIA at 1550 nm with ~3 mW of 770 nm light was approximately 130 dB/km. Then, several mW of 770 nm light reduces the RIA by 46×, relative to zero photobleaching. Thus, the high-dose RIA at 1550 nm in SMF28e+ fibers at 15 K can be reduced by well over an order of magnitude using relatively low intensities of 770 nm light.

More generally, the final primary RIA values decreased as the secondary wavelength decreased from 1050 nm to 770 nm, then increased significantly for λ_{PB} = 450 nm. The data suggest that higher photon energies are more effective at reducing RIA, but only up to some limit, and energies greater than this limit appear significantly worse at reducing RIA.

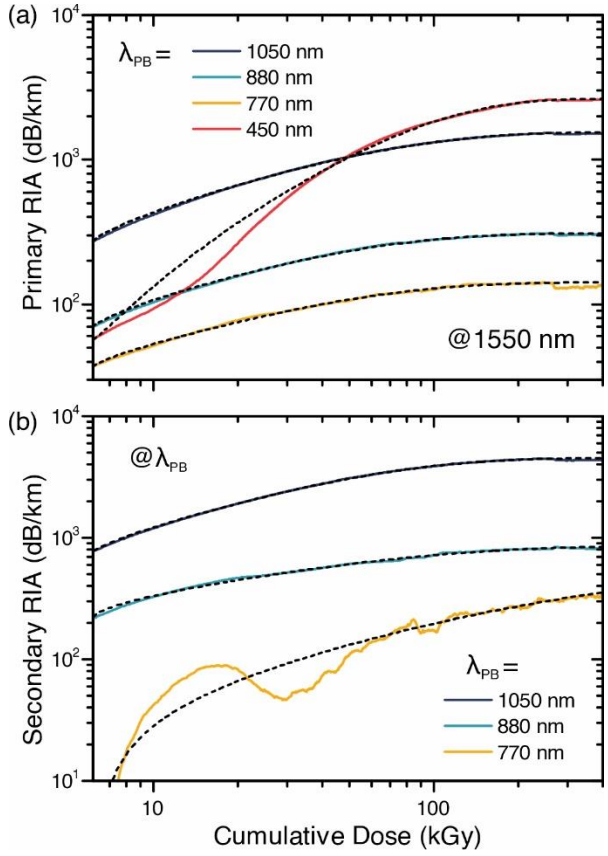

Fig. 4. (a) Primary RIA at 1550 nm as a function of cumulative dose, during the high-dose irradiation period. (b) Secondary RIA at the photobleaching wavelengths as a function of cumulative dose, during the high-dose irradiation period. Solid lines are experimental data; dashed lines are fits to (1).

To better understand this effect, we can consider the growth behavior of the primary RIA when λ_{PB} = 450 nm and compare it to the growth of the primary RIA for other, more effective photobleaching wavelengths. As noted earlier, the primary RIA when λ_{PB} = 450 nm was similar to that when λ_{PB} = 770 nm for small cumulative doses, and over an order of magnitude larger by the end of the irradiation (Table II). Furthermore, the RIA data are characterized by two major points of inflection: at 9 kGy, above which the RIA growth accelerates; and at 29 kGy, above which the RIA growth decelerates and trends toward saturation. Importantly, similar acceleration effects have been observed in longer fibers during photobleaching, and it was demonstrated that this feature appears when there is significant attenuation of the photobleaching light [19]. Thus, we must consider whether a similar effect occurs for λ_{PB} = 450 nm.

The photobleaching efficacy depends on the intensity of the photobleaching light [23]. Then, when the photobleaching light is attenuated via secondary RIA, the photobleaching efficacy will decrease along the length of fiber, and the primary RIA will correspondingly increase. This effect will become increasingly apparent in longer fibers. Our results

demonstrate that there is significant RIA at each secondary wavelength, and that the RIA is larger than that at the primary wavelength, such that this effect may be apparent.

We partially quantified the effects of fiber length on three of the four fibers studied in this work as follows. The actual losses (dB) at each secondary wavelength over the 2 m lengths of fiber were calculated from the final secondary RIA values (Table II). Then, relative to the pre-irradiation input powers (Table I), we determined that 14% of the 1050 nm light, 70% of the 880 nm light, and 86% of the 770 nm light, was transmitted post-irradiation. Consequently, despite the large RIA per unit length, significant intensities of photobleaching light were transmitted through each fiber, such that the photobleaching was generally effective.

We can consider a system in which the photobleaching light is entirely attenuated at some critical length L, such that there is non-zero photobleaching for $d < L$, and zero photobleaching for $d > L$. As conventional RIA measurements, like those presented herein, measure the RIA integrated along the length of fiber, it is not possible to distinguish the local RIA at each d. Alternative measurement techniques (e.g., FBG arrays) are required [19].

We attribute the behavior of the primary RIA where λ_{PB} = 450 nm to these length effects. Although we did not directly measure the secondary RIA at 450 nm, it is known that both the intrinsic fiber attenuation and the RIA are orders of magnitude more severe at visible wavelengths compared to 1550 nm [24, 25]. For small cumulative doses, the 450 nm light is effective at photobleaching due to strong transmission of the high energy light. However, as the irradiation continues, the attenuation at 450 nm increases significantly. At some intermediate dose on the order of 10 kGy, the 450 nm light is completely attenuated at some critical L, and zero photobleaching occurs beyond this length. Then, the integrated RIA increases rapidly. Notably, the saturated primary RIA (2590 dB/km) is still significantly less than that measured for zero photobleaching (6000 dB/km) due to the bleaching that occurs at $d < L$. A more thorough investigation of the effects of fiber length and photobleaching wavelength on the overall photobleaching efficacy will be the focus of a future work. Regardless, this qualitative description explains the several points of inflection in the primary RIA where λ_{PB} = 450 nm, and why 450 nm light is significantly less effective than 770 nm light.

A secondary purpose of this work was to compare the RIA measured at the primary and secondary wavelengths. The latter are not often measured in photobleaching studies, and comparing the growth rates and saturation RIA across wavelengths can provide information as to whether the RIA at different wavelengths manifests due to similar or distinct defects. To enable quantitative comparisons, the data in Fig. 4 were fit to stretched saturating exponentials, which are known to describe RIA growth curves with accuracy [26,27], of the form:

$$RIA(D) = RIA_0 + (RIA_{\mathrm{sat}} - RIA_0)\left(1 - \exp\left[-(k_{\mathrm{eff}}(D - D_s)^{\beta}\right]\right), \quad (1)$$

where RIA_0 is the RIA at the beginning of the high-dose irradiation period (i.e., the end of the late-stage seasoning

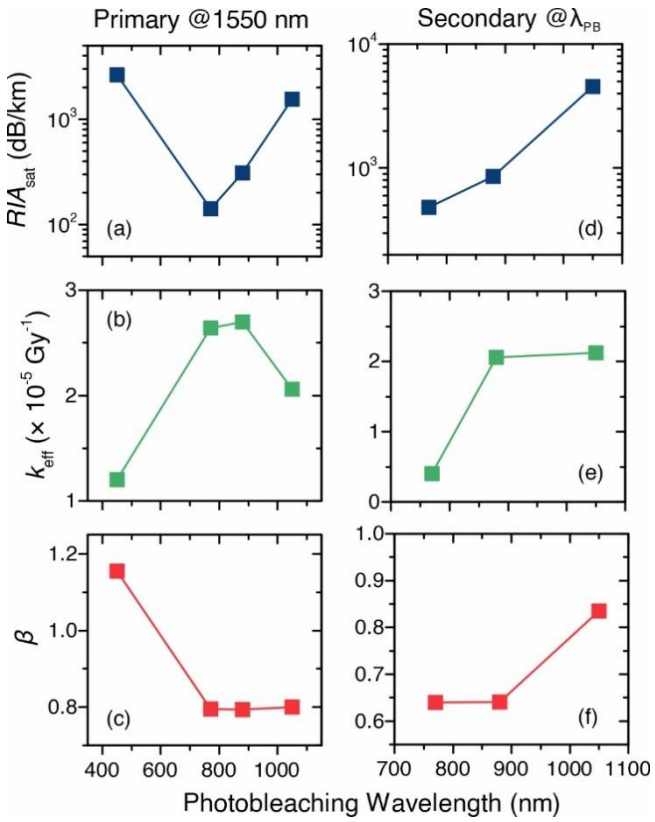

Fig 5. Fitted parameters using the data in Fig. 4 and (1) for each photobleaching wavelength: (a) RIA_{sat} at 1550 nm; (b) k_{eff} at 1550 nm; (c) β at 1550 nm; (d) RIA_{sat} at λ_{PB}; (e) k_{eff} at λ_{PB}; (f) β at λ_{PB}.

period), RIA_{sat} is the saturation RIA, k_{eff} is the effective defect activation rate, β is a stretching factor that manifests due to defect disorder, and D_s is the cumulative dose at the beginning of the high-dose irradiation period. The RIA_0 values are given in Table II and D_s = 6.01 kGy.

The primary RIA data were fit to (1) with good accuracy ($R^2 > 0.99$), though the fit failed to capture the low-dose (length-related) component for λ_{PB} = 450 nm. For λ_{PB} = 450 nm, the fitted values were up to 36% larger than the experimental values between 10 kGy and 70 kGy. For all other λ_{PB}, the fitted values were within ±6% of the experimental values over the entire fitted dose range. The secondary RIA data were also fit to (1) with good accuracy ($R^2 > 0.99$), though the fit for λ_{PB} = 770 nm was complicated by experimental noise at low doses. All data were fit from D_s up to 262 kGy to avoid fitting the experimental error discontinuity. The RIA_{sat}, k_{eff}, and β parameters extracted from each fit are presented in Fig. 5.

The fitted RIA_{sat} values were only slightly larger than the final RIA values at both the primary (Fig. 5a) and secondary (Fig. 5d) wavelengths (Table II), as all fibers were close to saturation. The activation rates at the primary wavelength varied with photobleaching wavelength (Fig. 5b) and were largest for λ_{PB} = 880 nm and 770 nm, and smallest for λ_{PB} = 450 nm. The stretching factors at the primary wavelength (Fig. 5c) were similar for all λ_{PB} except λ_{PB} = 450 nm which was larger and >1. The activation rates at the secondary wavelengths also varied with wavelength (Fig. 5e), and were

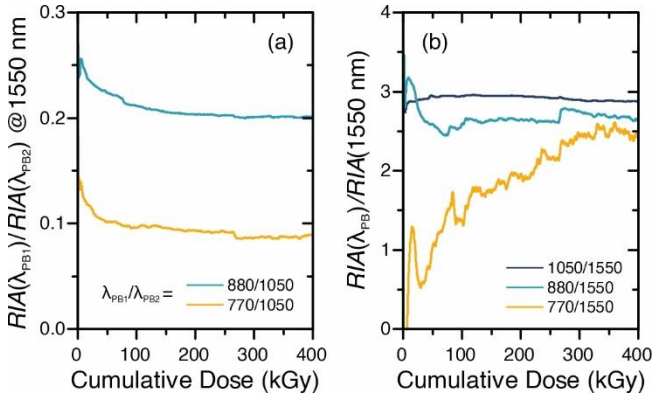

Fig. 6. (a) Ratio of the RIA at 1550 nm where λ_{PB} = 880 nm and λ_{PB} = 770 nm to the RIA at 1550 nm where λ_{PB} = 1050 nm. (b) Ratio of the RIA at the photobleaching wavelengths λ_{PB} = 1050 nm, λ_{PB} = 880 nm, and λ_{PB} = 770 nm to the RIA at 1550 nm for each λ_{PB}.

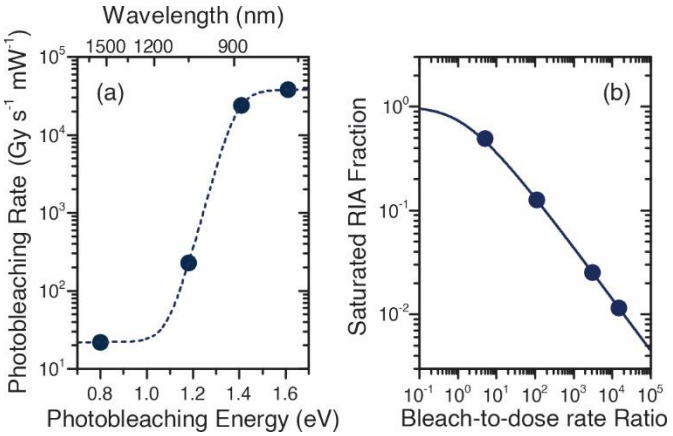

Fig. 7. (a) Calculated photobleaching factor α_λ versus the photobleaching energy. (b) Calculated (line) and experimental (symbols) saturation RIA fraction for SMF28e+ fibres at 15 K as a function of the bleach-to-dose rate ratio. The 1550 nm bleaching datapoint was obtained from [23].

similar at 1050 nm and 880 nm and smaller for 770 nm. Conversely, the stretching factors at the secondary wavelengths (Fig. 5f) were similar at 880 nm and 770 nm and larger at 1050 nm.

The k_{eff} and β values obtained from the primary RIA data were similar for all λ_{PB} = 1050 nm, 880 nm, or 770 nm. This suggests that the same defect, or convolution of defects, manifests the RIA at 1550 nm, regardless of the photobleaching energy. The same is likely true for λ_{PB} = 450 nm; however, both k_{eff} and β are heavily modified by the length effects discussed earlier. Thus, it is highly unlikely that the presence of photobleaching light changes the fundamental characteristics of the defects that dominate the absorption at 1550 nm at 15 K, despite the massive reduction in RIA. Rather, photobleaching simply affects the stable concentration of defects. This effect is clearly observed by taking the ratios of the primary RIA for different λ_{PB} (Fig. 6a), which are approximately constant in the high dose (>100 kGy) regime.

The k_{eff} and β values obtained from the secondary RIA data can then be compared to those obtained from the primary RIA data to evaluate whether similar or distinct defects are probed at each wavelength. For λ_{PB} = 1050 nm, both values were similar at both the primary and secondary wavelengths, suggesting that both wavelengths probe the same defect(s), albeit at different photon energies. Conversely, for λ_{PB} = 880 nm and 770 nm, both values were distinct across the primary and secondary wavelengths. This suggests that additional defect(s) absorb at shorter wavelengths, which must affect the photobleaching efficacy. This effect is clearly observed by taking the ratio of the secondary and primary RIAs (Fig. 6b). At λ_{PB} = 1050 nm, the ratio was approximately constant over the entire irradiation period. At λ_{PB} = 880 nm, the ratio was approximately constant after an initial period of irradiation (~50 kGy). At λ_{PB} = 770 nm, the ratio steadily increased over the entire irradiation period. However, in all cases the ratio at high doses appeared to saturate between 2 and 3. Ultimately, we conclude that the main defect manifesting RIA at 15 K must have a peak absorption below 1550 nm, toward the photobleaching wavelengths tested in this work.

We then quantified the photobleaching efficacy at each wavelength, independent of the experimental photobleaching intensities. This is complicated by the RIA growth and equilibrium dynamics that are intensity independent, as the photobleaching intensities were not exactly equivalent at each wavelength (Table I). However, in earlier works, we developed and validated an analytical model that successfully captures the interdependence between the dose rate, photobleaching power, and temperature on the saturation RIA in various fibers [22, 23]. We established that the photobleaching rate due to the 1550 nm probe light at ~1 mW is an order of magnitude smaller than the photobleaching rate of 1050 nm secondary light at a similar power in the same fibers irradiated at 15 K. We can then use the same model to calculate the photobleaching rates at the other wavelengths λ_{PB} = 880 nm and 770 nm. λ_{PB} = 450 nm is excluded from the analysis due to the length effects discussed earlier.

The photobleaching rates per mW of input power (α_λ) were calculated using the following relation:

$$RIA_{sat} = \frac{2RIA_T}{\left(1+\sqrt{1+\frac{2\alpha_\lambda P_\lambda}{\Phi}}\right)}, \quad (2)$$

where RIA_T is the saturation RIA at 1550 nm when there is no photobleaching (i.e., when P_λ = 0), RIA_{sat} is the saturation RIA at 1550 nm, P_λ is the photobleaching power, and Φ is the radiation dose rate. We earlier demonstrated that RIA_T = 12280 dB/km in SMF28e+ fibers [23].

The calculated α_λ at 1550 nm, 1050 nm, 880 nm, and 770 nm, as a function of photon energy, are presented in Fig. 7a. The photobleaching rate increased with energy, by approximately 1700× from 1550 nm to 770 nm. The energy dependence is characteristic of photoionization phenomena, where photons with energies above some threshold efficiently liberate trapped charges and consequently bleach the absorptive defect [28, 29]. Above the threshold, the

photoionization rate does not change significantly (i.e., for 880 nm and 770 nm).

Thus, it is unlikely that secondary wavelengths <770 nm would offer significant advantages in future photobleaching systems. Conversely, shorter wavelengths will be more severely attenuated by additional short-wavelength absorptive defects unrelated to the attenuation at 1550 nm, such that the photobleaching efficacy would more likely decrease. We conclude that secondary wavelengths near 770 nm will be optimal for reducing cryogenic RIA at 1550 nm.

Finally, to inform the development of new cryogenic fiber systems with photobleaching for radiation-rich environments, it is of interest to consider how the photobleaching rates will ultimately affect the saturation RIA over a broad range of photobleaching powers, wavelengths, and dose rates. Per (2), RIA_{sat} decreases as the ratio of the experimental inputs $\alpha_\lambda P_\lambda/\Phi$ increases. The calculated RIA fraction, RIA_{sat}/RIA_T, which conveys the overall reduction in the high-dose RIA for non-zero photobleaching, as a function of the bleach-to-dose rate ratio ($\alpha_\lambda P_\lambda/\Phi$) is shown in Fig. 7b. The functional form of (2) ultimately implies diminishing returns for larger bleach-to-dose rate ratios. Practically, this means that, in situations where fibers are exposed to very high dose rates, a directly proportional amount of photobleaching power must be injected to maintain the same RIA fraction. As very high photobleaching powers will induce undesirable non-linear effects (e.g., multi-photon-induced defect production and stimulated scattering effects [30,31]), the efficacy of photobleaching as an RIA reduction mechanism is effectively capped. This limitation will be further compounded by length effects, related to the attenuation of the photobleaching light, at higher dose rates. Regardless, in the length independent limit (i.e., for short fibers and/or large photobleaching powers), the model enables one to calculate the optical power required to maintain the RIA below some pre-defined threshold, provided the wavelength-dependent photobleaching rate is known. Thus, the α_λ values presented in this work will facilitate the development of new fiber sensing systems designed to operate in radiation-rich environments.

V. Conclusion

In this work, we investigated the influence of different photobleaching wavelengths (1050 nm, 880 nm, 770 nm, and 450 nm) on the RIA of germanosilicate fibers irradiated at 15 K. The RIA was measured at the primary wavelength 1550 nm and at the secondary photobleaching wavelengths, and the photobleaching intensities were similar at all wavelengths. We found that the 770 nm light reduced the high-dose (saturated) primary RIA by a factor of 10, relative to 1050 nm light, and a factor of approximately 50, relative to zero-photobleaching. We thus demonstrated that the wavelength (energy) of the secondary light has a massive effect on the photobleaching efficacy. We found that a shorter wavelength (i.e., 450 nm) was initially effective at reducing RIA at low doses, but less effective than all other wavelengths at high doses. We attributed this effect to attenuation of the photobleaching light by additional defects that do not contribute the primary RIA. We thus established that the optimal photobleaching wavelength for germanosilicate fibers must be near 770 nm. We compared the growth curves of the primary and secondary RIA for different secondary wavelengths (≥770 nm) and found that the high dose RIA at the secondary wavelength was 2–3× larger than that at the primary wavelength. Thus, we establish that a similar convolution of defects is responsible for the RIA at both the primary and secondary wavelengths, and that this defect must exhibit at least one absorption peak <1550 nm. Finally, we used a recently developed kinetic model to calculate the intensity-independent photobleaching rates for the different secondary wavelengths. The photobleaching rates at 770 nm and 880 nm were 1700× and 1100×, respectively, larger than the primary photobleaching rate at 1550 nm. These results will aid in the design of efficient and effective radiation-resistant cryogenic fiber optic sensing systems.

References

[1] S. Girard *et al*., "Overview of Radiation Effects on Silica-Based Optical Fibers and Fiber Sensors", *IEEE Trans. Nucl. Sci.*, vol. 72, no. 4, pp. 982-1020, April 2025.

[2] F.S. Fernandez *et al*., "Photobleaching of Neutron Radiation Induced Attenuation of Optical Fibers at Liquid Nitrogen Temperature", *IEEE Trans. Nucl. Sci.*, vol. 72, no. 7, pp. 2145-2153, July 2025.

[3] M. Roche *et al*., "Temperature Dependence of the Radiation Response of Ultralow-Loss Optical Fibers: Role of Self-Trapped Holes", *IEEE Trans. Nucl. Sci.*, vol. 72, no. 4, pp. 1165-1171, April 2025.

[4] I. Toccafondo *et al*., "Irradiation of Multimode Ge-doped and F-doped Optical Fibers at Cryogenic Temperatures Down to 10 K", *Journal of Lightwave Technology*, vol. 41, no. 1, pp. 286-292, Jan. 2023.

[5] P.F. Kashaykin, E.A. Pospelova, Y.O. Sharonova, O.L. Vokhmyanina, I.S. Azanova, A.L. Tomashuk, "Temperature and polarization dependence of radiation-induced attenuation in pure-silica-core PANDA optical fiber", *Optical Materials*, vol. 131, Sep. 2022, Art. no. 112510.

[6] C. Campanella, *et al*., "Temperature Dependence of Radiation Induced Attenuation of Aluminosilicate Optical Fiber", *IEEE Trans. Nucl. Sci*. vol. 69, no. 7, pp. 1515-1520, July 2022.

[7] J. Blanc, D. Ricci, J. Kuhnhenn, U. Weinand, O.J. Schumann, "Irradiation of radiation-tolerant single-mode optical fibers at cryogenic temperature", *Journal of Lightwave Technology*, vol. 35, no. 10, pp. 1929-1935, May 2017.

[8] J. Kuhnhenn, O.J. Schumann, U. Weinand, R. Wolf, "Gamma Irradiation Test of Ge-Doped Single- Mode Optical Fiber at Cryogenic Conditions", in *RADECS, IEEE*, Bremen, Germany, Sept. 2016, pp. 1-4.

[9] B.M. Ludbrook *et al*., "Resilience of Fiber-Bragg Grating Optical Sensors under Neutron Irradiation at 77 K", *IEEE Trans. Appl. Supercond*., vol. 35, no. 5, Aug. 2025, Art no. 9000105.

[10] C G. Colombo *et al*., "Fiber-Optics Quench Detection Schemes in HTS Cables for Fusion Magnets", *IEEE Trans. Appl. Supercond*., vol. 34, no. 5, Aug. 2024, Art. no. 4702305.

[11] S. Girard *et al*., "Recent advances in radiation-hardened fiber-based technologies for space applications", *Journal of Optics*, vol. 20, Aug. 2018, Art. no. 093001.

[12] M. Roche *et al*., "Temperature Cycling Effects on Infrared Radiation-Induced Attenuation of Silica-Based Optical Fibers", *IEEE Trans. Nucl. Sci*., vol. 71, no. 4, pp. 744-751, April 2024.

[13] A. Morana *et al*., "Temperature Dependence of Radiation-Induced Attenuation of a Fluorine-Doped Single-Mode Optical Fiber at Infrared Wavelengths", *IEEE Trans. Nucl. Sci*., vol. 70, no. 4, pp. 549-555, April 2023.

[14] J. Li *et al*., "Radiation Damage Mechanisms and Research Status of Radiation-Resistant Optical Fibers: A Review", *Sensors*, vol. 24, no. 10, 2024, Art. no. 3235.

[15] F. Solis Fernandez *et al*., "Mitigation of radiation-induced attenuation of optical fibers through photobleaching: study of power dependence at cryogenic temperatures", in Proc. SPIE 12949, SPIE Smart Structures, Long Beach, Calif., USA, March 2024, Art. no. 129490A.

[16] F. Solis Fernandez *et al*., "Mitigation of high X-ray dose radiation-induced attenuation in optical fibers at 15 K: effect of cumulative dose", *Optical Engineering*, vol. 64, no. 7, July 2025, Art. no. 076101.

[17] M. Roche *et al*., "Combined Photobleaching and Temperature Effects on 1550 nm Radiation-Induced Attenuation of Germanosilicate Optical Fiber", *IEEE Trans. Nucl. Sci.*, vol. 70, no. 8, pp. 1951-1957, Aug. 2023.

[18] A. Morana *et al*., "Photobleaching Effects on the Radiation-Induced Attenuation of Germanosilicate Optical Fibers at Low Temperature", *IEEE Trans. Nucl. Sci.*, vol. 72, no. 8, pp. 2548-2554, Aug. 2025.

[19] O. Duke, J. Desroches, E. Salazar, "Length-Resolved Measurement of Radiation Induced Attenuation in Quench Detection Optical Fibers with Photobleaching", *IEEE Trans. Appl. Supercond.*, vol. 35, no. 5, Aug. 2025, Art. no. 9500504.

[20] O. Duke, A. Greenberg, J. Desroches, J. Schuyt, D. Moseley, E. Salazar, "Reducing Radiation Effects on Fiber Optic Quench Detection Sensors with Optical Annealing", *IEEE Trans. Appl. Supercond.*, vol. 34, no. 5, Aug. 2024, Art. no. 9001904.

[21] C.E. Barnes, "Laser diode-induced photobleaching at low temperature in Co-60 irradiated fibers", *IEEE Trans. Nucl. Sci.*, vol. 29, no. 6, pp. 1479-1483, Dec. 1982.

[22] J.J. Schuyt, D.A. Moseley, B.M. Ludbrook, S.M. Haneef, R.A. Badcock, "Modeling the Radiation-induced Attenuation Limits in Optical Fibers During Concurrent Irradiation, Thermal Annealing, and Photobleaching", *IEEE Trans. Nucl. Sci.*, vol. 72, no. 7, pp. 2154-2162, July 2025.

[23] F.S. Fernandez, J.J. Schuyt, S.M. Haneef, D.A. Moseley, B.M. Ludbrook, R.A. Badcock, "Radiation-induced Attenuation in Standard Optical Fibers at Cryogenic Temperatures: Dose Rate, Temperature, and Photobleaching Interdependence", *Journal of Lightwave Technology* (early access, doi: 10.1109/JLT.2025.3640537)

[24] C. Campanella *et al*., "Influence of Ambient Light on the Radiation-Induced Attenuation of Germanosilicate Optical Fibers in the Visible and Near-Infrared Domains", *IEEE Trans. Nucl. Sci.*, vol. 70, no. 4, pp. 562-567, April 2023.

[25] A. Anedda, C.M. Carbonaro, R. Corpino, A. Serpi, "Absorption spectrum of Ge-doped silica samples and fiber preforms in the vacuum ultraviolet region", *J. Non Cryst. Solids.*, vol. 280, pp. 281-286, Feb. 2001.

[26] D.L. Griscom, "Fractal kinetics of radiation-induced point-defect formation and decay in amorphous insulators: Application to color centers in silica-based optical fibers", *Phys. Rev. B*, vol. 64, no. 17, Oct. 2001, Art. no. 174201.

[27] J.J. Schuyt, O. Duke, D.A. Moseley, B.M. Ludbrook, E.E. Salazar, R.A. Badcock, "Gamma irradiation of Ge-doped and radiation-hard silica fibers at cryogenic temperatures: Mitigating the radiation-induced attenuation with 1550 and 970 nm photobleaching", *J. Appl. Phys.*, vol.134, no. 4, July 2023, Art. no. 043103.

[28] J.M. Noras, "Photoionisation and phonon coupling", *J. Phys. C: Solid St. Phys.*, vol. 13, no. 25, pp. 4779–4789, Sep. 1980.

[29] A. Chruścińska, P. Palczewski, "OSL characteristics: Theory and experiments", *Radiat. Prot. Dosimetry*, vol. 192, no. 2, pp. 266-293, Nov. 2020.

[30] Q. Li, H. Zhang, X. Shen, P. Yan, H. Hao, M. Gong, "Stimulated Raman scattering threshold for partially coherent light in silica fibers", *Optics Express*, vol. 23, no. 22, pp. 28438-28448, Nov. 2015.

[31] T. Sun, X. Su, Y. Zhang, H. Zhang, Y. Zheng, "Progress and summary of photodarkening in rare earth doped fiber", *Applied Sciences*, vol. 11, no. 21, 2021, Art. no. 10386.